ACS OMEGA

Open Access

http://pubs.acs.org/journal/acsodf

Article

Surface Nanostructures Enhanced Biocompatibility and Osteoinductivity of Laser-Additively Manufactured CoCrMo Alloys

Kun Man, Sangram Mazumder, Narendra B. Dahotre,* and Yong Yang*

Cite This: *ACS Omega* 2023, 8, 47658−47666

Read Online

ACCESS | Metrics & More | Article Recommendations | Supporting Information

ABSTRACT: Cobalt−chromium−molybdenum (CoCrMo) alloys are widely used in orthopedic implants due to their excellent corrosion and wear resistance and superior mechanical properties. However, their limited capability to promote cell adhesion and new bone tissue formation, poor blood compatibility, and risk of microbial infection can lead to implant failure or reduced implant lifespan. Surface structure modification has been used to improve the cytocompatibility and blood compatibility of implant materials and reduce the risk of infection. In this study, we prepared CoCrMo alloys with surface nanostructures of various aspect ratios (AR) using laser-directed energy deposition (L-DED) and biocorrosion. Our results showed that medium and high AR nanostructures reduced platelet adhesion, while all of the alloys demonstrated good blood compatibility and antibacterial properties. Moreover, the medium and high AR nanostructures promoted cell adhesion and spreading of both preosteoblast MC3T3 cells and human bone marrow mesenchymal stem cells (hMSCs). Furthermore, the nanostructure promoted the osteogenic differentiation of both cell types compared with the flat control surface, with a substantial enhancing effect for the medium and high ARs. Our study proposes a promising approach for developing implant materials with improved clinical outcomes.

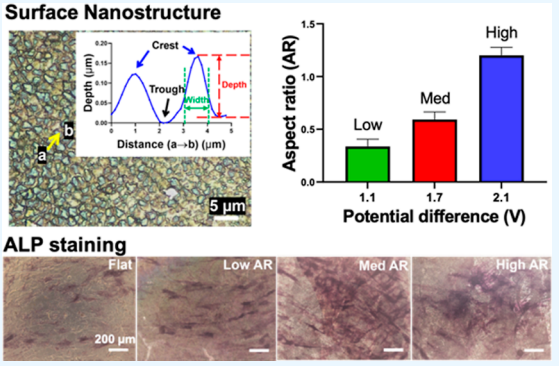

1. INTRODUCTION

Orthopedic implants have become an indispensable solution for restoring the functionality of bones and joints in individuals suffering from joint problems such as osteoarthritis and rheumatoid arthritis, thus improving the quality of life. The US orthopedic implants market has experienced significant growth, with a value of $46.5 billion in 2018, and is projected to reach $64 billion by 2026.[1] Metallic materials, such as titanium, stainless steel, and cobalt−chromium (CoCr) alloy, have shown promise for bone tissue regeneration and orthopedic implants due to their high strength and durability compared with other materials such as ceramics or polymers.[2−5] Among these materials, cobalt−chromium−molybdenum (CoCrMo) alloy has been widely used in orthopedic applications, such as hip replacement, due to its high corrosion resistance, wear resistance, strength, and hardness.[6−9] However, metallic implants' blood compatibility, anti-infection properties, and limited capability to promote cell adhesion and new bone tissue formation pose great concerns that may lead to implant failure or reduce the implant lifetime.[10,11]

To address these challenges, researchers have explored various approaches, including compositional and structural modifications.[10−14] Surface structure modification, in particular, offers a more stable and controllable way to promote implant performance without inducing additional ion release or detrimental interactions with physiological fluids.[15,16] Recently, the biocompatibility of implanted materials has been widely investigated in relation to the influence of their surface topography, with a focus on crucial interactions for long-term performance.[17,18] Notably, nanotube structure on the titanium oxide (TiO_2) surface has been reported to boost osteoblast growth by 300−400% compared to flat control.[18] A variety of surface modification methods have been employed, such as physical vapor deposition, electrochemical deposition, biomimetic coating, and laser surface texturing. Among these methods, selective laser melting and laser-directed energy deposition (L-DED) have been reported to fabricate the CoCrMo alloy. In comparison with other approaches, L-DED offers several advantages, including enhanced long-term stability, reduced risk of coating delamination, improved corrosion resistance, and the ability to create implants with complex structures directly.[19−21] Our previous study revealed that the extremely high cooling rates during the L-DED process resulted in the formation of a fine subgrain morphology and nonuniform distribution of Co and Mo, which facilitated the generation of stable surface nanostruc-

Received: August 8, 2023
Accepted: September 19, 2023
Published: December 6, 2023

tures with different aspect ratios (AR) through selective etching during the subsequent potentiodynamic polarization (PDP) process. Our preliminary study showed that these surface nanostructures promoted adhesion and proliferation of preosteoblast MC3T3 cells.[22]

In this study, we investigated the effects of nanostructured CoCrMo alloys in bone tissue engineering. We investigated the effects of the alloy surface nanostructures on blood compatibility and antibacterial properties that are crucial for implants. As bone formation at the implant surface involves preosteoblast and human bone marrow mesenchymal stem cell (hMSC) adhesion, proliferation, osteogenic differentiation, and subsequent synthesis of bone matrix,[23−25] we further evaluated the effects of the nanostructure on MC3T3 cells and hMSC behavior in terms of cell adhesion, spreading, and osteogenic differentiation.

2. EXPERIMENTAL SECTION

2.1. Fabrication of CoCrMo Alloys with the Surface Structure. The CoCrMo alloy was first prepared by the L-DED process using Ambit Mini Mill system equipped with a Nd/YAG laser (1.06 μm wavelength), as previously reported.[19] Commercially available CoCrMo alloy powder was melted at the focal plane of the laser beam (550 W laser power, 1 mm in diameter) using argon as the carrier gas and deposited onto the substrate at a linear velocity of 15 mm/s. A laser scanning pattern was employed with a 0.6 mm overlap between consecutive laser tracks and a 90° rotation after each layer. The resulting L-DED CoCrMo alloys were sectioned in the *YZ* plane (plane parallel to the build direction), polished, and subjected to PDP biocorrosion. The VSP 300 potentiostat/galvanostat (Bio-Logic, Seyssinet-Pariset, France) was used to perform PDP biocorrosion with simulated body fluid (SBF) as the electrolyte. The biocorrosion was conducted at 37 °C with various potential differences to create surface nanostructures of different depths.[22]

Conventionally cast CoCrMo alloys, followed by homogenization heat-treated, were used as a flat control with a homogeneous elemental distribution. All alloys were sterilized using an autoclave and rinsed with PBS before use.

2.2. Characterization of the CoCrMo Alloys. The morphology of the CoCrMo alloys was examined using scanning electron microscope (SEM) and optical microscope. SEM images were captured using FEI Nova 230, and optical microscopic images were taken using Zeiss Axiolab 5 (Carl Zeiss Meditec, Jena, Germany). The elemental composition of the alloys was determined using energy-dispersive X-ray spectrometer (EDS), which was performed using FEI ESEM Quanta. Surface profilometry analysis of the CoCrMo alloys after biocorrosion was performed using a VK-X1000 surface profiler equipped with a laser microscope (Keyence, Osaka, Japan). The width of the crests (determined as the full width at half-maximum) and depth of the throughs were measured from the surface profiles, and the AR of the surface nanostructures was determined by calculating the ratio of the average depth to the width.

2.3. Blood Compatibility. *2.3.1. Platelet Adhesion.* Each sample was fully covered with 200 μL/cm^2 platelet-rich plasma (PRP) (Zen-Bio, Research Triangle, NC, US) and incubated at 37 °C for 1 h. After removing nonadherent platelets by rinsing the samples with PBS, the samples were fixed with 4% paraformaldehyde (PFA; Sigma-Aldrich, St Louis, MO, USA) and 2% glutaraldehyde solution (Fisher Chemical, Fair Lawn, NJ, US) at room temperature for 2 h. The fixed samples were dehydrated using a gradient of ethanol (30, 50, 70, 80, 90, 95, and 100%) and then hexamethyldisilazane (HMDS), with each step taking 10 min. The samples were stored in a desiccator and sputter-coated with gold using a Denton Vacuum Desk V sputter coater (Denton Vacuum, Moorestown, NJ, USA) before SEM observation using FEI Quanta 200 ESEM. Adhered platelets were counted from SEM images.

2.3.2. Hemolysis Test. Healthy human blood containing 3.8% sodium citrate (Zen-Bio, US) was diluted with 0.9% sodium chloride solution (4:5, v/v). Each sample was immersed in a 15 mL centrifuge tube containing 9.8 mL of 0.9% sodium chloride solution and incubated at 37 °C for 30 min. Subsequently, 200 μL of diluted blood was added to each tube and incubated at 37 °C for 1 h. The tubes were then centrifuged at 3000 rpm for 5 min, and the absorbance (A) of the supernatants was measured at the wavelength of 545 nm using a Cytation 5 Cell Imaging Multi-Mode Reader (BioTek, Winooski, VT, USA). A positive control was prepared by adding diluted blood to 9.8 mL of deionized water, and a negative control was prepared using 0.9% sodium chloride solution. The hemolysis ratio (HR) was calculated using the following equation

$$\mathrm{HR}(\%) = (A_{\mathrm{sample}} - A_{\mathrm{negative}})/(A_{\mathrm{positive}} - A_{\mathrm{negative}}) \times 100\%$$

2.4. Antibacterial Properties. *Escherichia coli* (ATCC 25922, US) were cultured in Tryptic Soy Broth (TSB; BD, Franklin Lakes, NJ, US) at 37 °C and 200 rpm until the bacterial concentration reached approximately 10^8 colony-forming units (CFU)/mL. The bacterial solution was then diluted 10-fold using TSB to a concentration of 1×10^4 CFU/mL. The samples were placed in separate Petri dishes, and 0.2 mL/cm^2 of the bacterial suspension was dipped onto the samples. A negative control was prepared by dipping the bacterial suspension onto Tryptic Soy Agar (TSA; BD) spread in a Petri dish. All the dishes were placed in wet chambers and incubated at 37 °C for 24 h. After incubation, the bacteria were collected by washing the samples with PBS (2 mL/cm^2) and diluted 1000-fold. Then, 10 μL of the solution was inoculated onto TSA plates and incubated at 37 °C for 18 h. The bacteria colonies were counted, and the antibacterial activity (R) was calculated using the following formula

$$R = (N_{\mathrm{negative}} - N_{\mathrm{sample}})/(N_{\mathrm{negative}}) \times 100\%$$

where N_{negative} and N_{sample} were the colony numbers on the negative control and alloy samples, respectively.

2.5. Cell Culture. Murine calvarial preosteoblasts (MC3T3-E1; ATCC CRL-2593, US) were cultured in α-minimum essential medium (α-MEM; Gibco, Grand Island, NY, USA) supplemented with 10% fetal bovine serum (FBS; Sigma-Aldrich, St Louis, MO, USA), 100 U/mL penicillin, and 100 μg/mL streptomycin (Life Technologies, Carlsbad, CA, USA). The hMSCs (Lonza, Bend, OR, USA) were cultured in mesenchymal stem cell growth medium (MSCGM, Lonza). The cells were seeded onto the samples at a density of 10,000 cells/cm^2 (unless otherwise specified) and cultured at 37 °C and 5% CO_2.

2.6. Immunofluorescence Staining. After 5 days of culture, the samples were rinsed gently with PBS and fixed with 4% PFA (Sigma-Aldrich) solution for 20 min at room temperature. The samples were then rinsed three times with

https://doi.org/10.1021/acsomega.3c04305
ACS Omega 2023, 8, 47658−47666

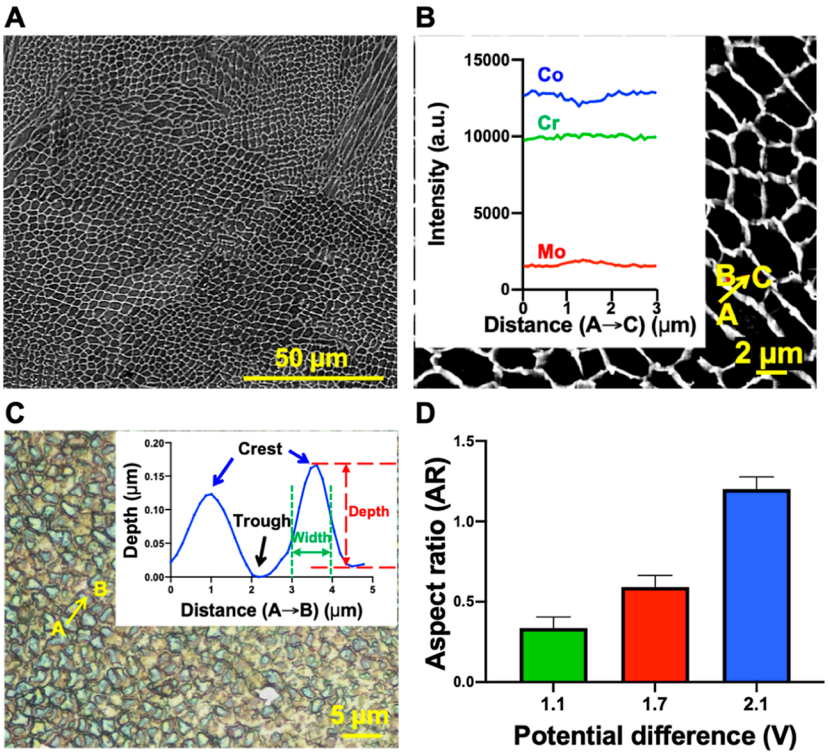

Figure 1. Characterization of the CoCrMo alloys. (A) Representative SEM image showing the microstructure of the L-DED-fabricated CoCrMo alloys. (B) SEM EDS line scan along two adjacent subgrains revealing a selective distribution of Mo and Co at the boundaries. (C) Representative optical microscopic image and laser surface profilometry analysis (inset) of the CoCrMo after PDP biocorrosion. (D) ARs of the surface nanostructures, corresponding to low AR (0.3), Med AR (0.6), and High AR (1.2) with increasing potential difference during the PDP biocorrosion process. n = 70−100.

PBS and blocked for 1 h at room temperature using PBST solution (PBS supplemented with 0.2% Triton X-100) containing 0.03 g/mL bovine serum albumin (BSA; Sigma-Aldrich) and 0.1% goat serum (v/v, Sigma-Aldrich). Subsequently, the samples were incubated with Alexa Fluor 488 phalloidin (1:200, Life Technologies) and anti-paxillin antibody from rabbit (1:150, Abcam, Waltham, MA, USA) in PBST at 4 °C overnight. After being rinsed three times with PBS, the samples were incubated with Alexa Fluor 555 goat antirabbit secondary antibody (1:200, Life Technologies) at room temperature for 1 h. The nuclei were then stained with SlowFade Gold Antifade Mountant with 4,6-diamidino-2-phenylindole (DAPI) (Life Technologies), and the images were taken using a Zeiss LSM710 Confocal Microscope (Carl Zeiss). The fluorescence intensity, size, and number of paxillins per cell were analyzed using ImageJ.

2.7. Cell Morphology SEM Observations. After 5 days of culture, the samples were prepared using the same method as described in 2.3.1 for SEM observation and observed under an FEI Quanta 200 ESEM.

2.8. Spinning Disc Assay. The samples were placed in a 100 mm Petri dish and covered with poly(dimethylsiloxane) (PDMS; Sylgard 184, Ellsworth Adhesives, Germantown, WA, USA) to match the thickness of the samples. The PDMS was then cured at 75 °C for 2 h, and the samples were removed from the dish and used for cell culture. MC3T3 cells were seeded onto the samples at a density of 5000 cells/cm^2 and cultured for 1 day. The samples were then remounted back into the dish. The petri dish was covered with 1 mL of PBS and subjected to shear stress by spinning the dish at room temperature using a spin coater (Laurell 650 series; Laurell Technologies Corporation, Lansdale, PA, USA), as shown in Figure S1 in the Supporting Information. Three different shear stresses were generated at 500, 1000, and 1500 rpm for 2 min. Shear stresses were calculated using the following equation

$$\tau = 0.8r(\rho\mu\omega^3)^{1/2}$$

where τ is the shear stress, r is the radial position of the samples (0.04 m), ρ (997 kg/m^3) and μ (10^{-3} kg/m s) are the density and dynamic viscosity of PBS, and ω is the angular speed.[26]

Cell images were obtained using a Nikon Ti Eclipse microscope (Nikon, Melville, NY, USA) before and after spinning. The number of adherent cells was counted from at least four fields with a total of 70−250 cells for each sample.

2.9. Osteogenic Differentiation. After 21 days of culture, the cells were fixed with 4% PFA for 1 h and then stained with 5-bromo-4-chloro-3-indolyl phosphate and nitroblue tetrazolium (BCIP/NBT; VWR international, Radnor, USA) at room temperature for 20 min and then rinsed with deionized water until the background was clear for alkaline phosphatase (ALP) staining. In addition, after fixation, the cells were stained with alizarin-red S solution (1% in deionized water, Sigma-Aldrich) for 20 min and rinsed with deionized water until the background was clear. Images were taken using a Keyence BZ-X810 fluorescence microscope (Keyence, Osaka, Japan). The ALP activity was determined via colorimetry using an ALP assay kit (Abcam) according to the manufacturer's protocol. Briefly, the cells were harvested and lysed using the ALP assay buffer. Then, the cell lysate was incubated with p-nitrophenyl phosphate (pNPP) for 1 h, and the absorbance was measured at 405 nm. The protein concentration was measured using a

https://doi.org/10.1021/acsomega.3c04305
ACS Omega 2023, 8, 47658−47666

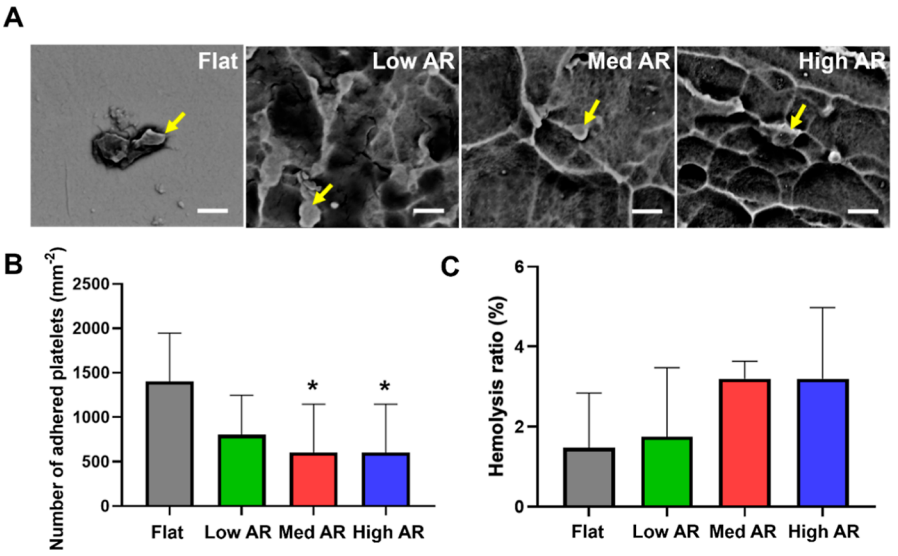

Figure 2. Blood compatibility of CoCrMo alloys with various surface structures. (A) SEM images of adherent platelets on the alloy surfaces. The yellow arrowheads indicate platelets. Scale bars: 10 μm. (B) Quantification of the number of adhered platelets on the alloys. (C) Hemolysis ratio of human blood incubated with the alloys. $n = 3$. *: $p < 0.05$ compared to the flat control surface.

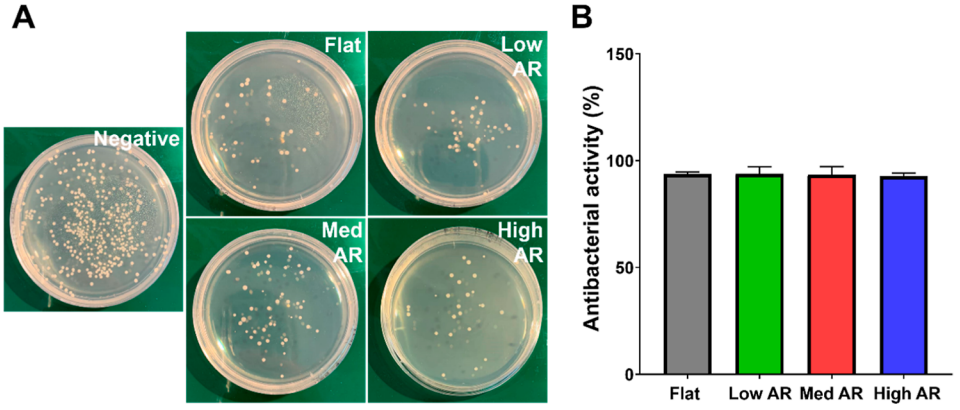

Figure 3. Evaluation of antibacterial properties of the alloys. (A) Optic images of colonization by *E. coli* on the negative sample and alloy surfaces. (B) Antibacterial activity of the alloys. $n = 3$.

standard bicinchoninic acid (BCA) Protein Assay Kit (Thermo Fisher Scientific, Cleveland, OH, USA), and the ALP activity was normalized to the protein quantity.

2.10. Statistical Analysis. Data were reported as mean ± standard errors except for the paxillin area data, which were presented as median with interquartile range. The statistical significances were analyzed based on two-tailed *t*-test with Welch's correction for all other data and two-tailed Mann−Whitney test for paxillin area data using Prism 8 (GraphPad software, San Diego, CA, US), with the significance level defined as $p < 0.05$.

3. RESULTS AND DISCUSSION

3.1. Fabrication and Characterization of the CoCrMo Alloy with Surface Nanostructures. The CoCrMo alloy was fabricated using the L-DED process, a commonly used additive manufacturing technique due to its high weldability and availability of precursor materials in powder or wire form. The resulting alloy exhibited a fine subgrain morphology, as shown in Figure 1A. Through SEM EDS line scanning across adjacent subgrains, a selective distribution of Mo and Co was observed, with relatively higher Mo concentration and lower Co concentration at the boundaries, as depicted in Figure 1B. This distribution facilitated the targeted etching of Co-rich cores during the subsequent PDP biocorrosion process.

After PDP biocorrosion, the CoCrMo alloy surface exhibited Mo-rich crests and Co-rich troughs, as observed through optical microscopy and surface profilometry measurements (Figure 1C). The width of the crests was measured to be 510 ± 97 nm from the profilometry measurement. The depth of the troughs increased with the applied potential difference during PDP biocorrosion. The aspect AR of the surface nanostructures was determined by the ratio of the average depth to the width. When the potential difference of 1.1, 1.7, and 2.1 V was applied, the through depth was 172 ± 35 nm, 302 ± 37 nm, and 612 ± 39 nm, respectively, resulting in low AR (0.3), Med AR (0.6), and High AR (1.2), as shown in Figure 1D.

3.2. Blood Compatibility. Platelet adhesion and hemolysis tests were conducted to evaluate the blood compatibility of the nanostructured CoCrMo alloys with different ARs, as well as a flat control surface. Platelet morphology and numbers adhered to the alloy surfaces are shown in Figure 2A,B, respectively. While platelet spreading and aggregation were

https://doi.org/10.1021/acsomega.3c04305
ACS Omega 2023, 8, 47658−47666

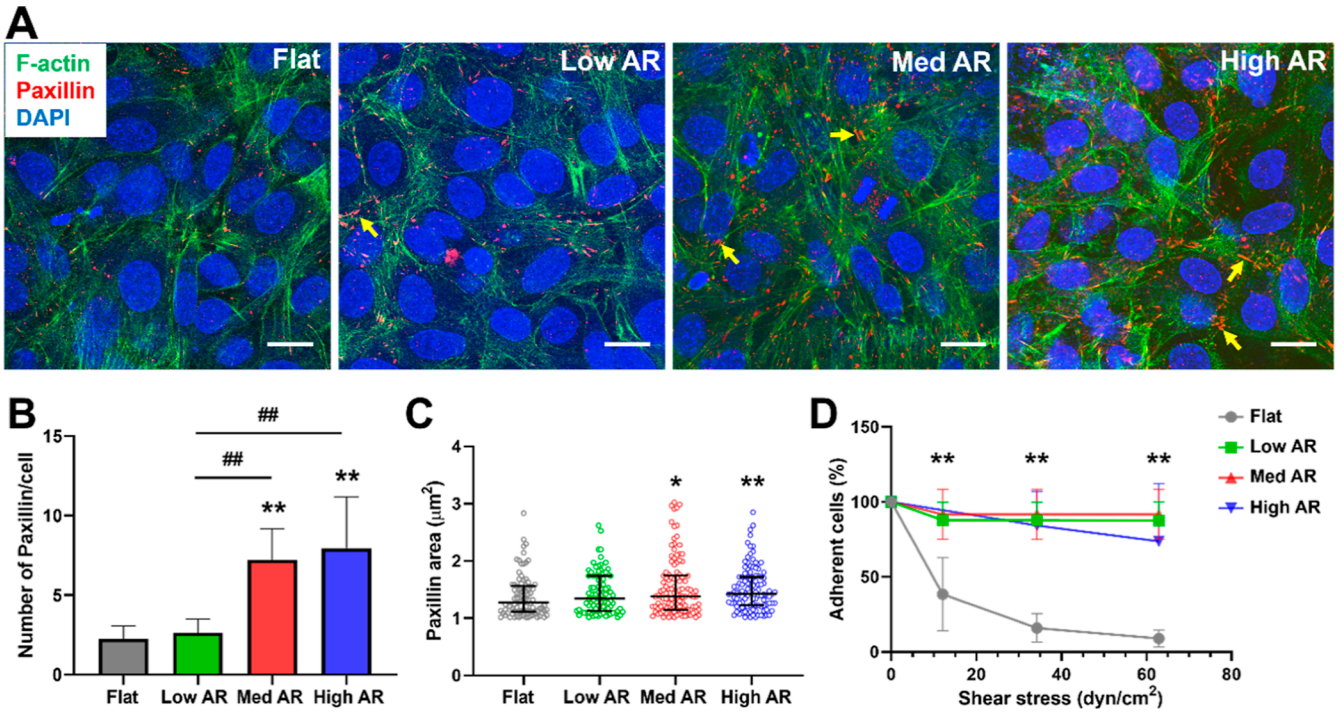

Figure 4. Adhesion and spreading of preosteoblasts MC3T3 on the samples. (A) Representative immunofluorescence images of the cells. The yellow arrows indicate mature paxillin. Scale bars: 20 μm. (B) Paxillin number per cell and (C) paxillin size analyzed from immunofluorescence images. n = 70−120. (D) Percentage of adherent cells as a function of applied shear stress. n = 80−200. *: $p < 0.05$, **: $p < 0.01$ compared to flat surface. #: $p < 0.05$, ##: $p < 0.01$ between groups.

observed on the flat control surface, the platelets displayed a round-shaped morphology and no aggregation on the nanostructured alloy surfaces. Moreover, the number of adhered platelets on medium and high AR alloys significantly lower than that on the flat surface. Minimizing platelet adhesion, spreading, and aggregation is essential to reduce thrombosis in biomedical materials. Additionally, hemolysis, defined as the damage of erythrocytes with the release of hemoglobin into the plasma, was evaluated. The hemolysis ratios of human blood incubated with all the alloys were less than 5% (Figure 2C), which is the permissible limit for blood-containing biomaterials according to ASTM F 756-08. These results demonstrated that the presence of medium and high AR nanostructures improved the blood compatibility of the CoCrMo alloy.

3.3. Antibacterial Properties. Bacterial infection is a common cause of implantation failure, and *E. coli* is one of the most prevalent causes of implant-associated infections.[27,28] Thus, the antibacterial properties of the alloys were assessed using the plate-count method with *E. coli*. The *E. coli* suspension was first incubated on the alloy surface or TSA plates (negative control) and then transferred onto TSA plates for further incubation for 18 h. Figure 3A shows representative *E. coli* colonies on the final TSA plates, with more colonies observed on the negative plate than on any of the alloy surfaces. The antibacterial activities of the alloys were also calculated and are presented in Figure 3B. All CoCrMo alloys, including the flat and nanostructured surfaces, exhibited antibacterial activities of over 90%, indicating their strong antibacterial properties.

The antibacterial properties of alloys are influenced by various chemical and physical properties, such as composition, packing, density, configuration, and surface topographies.[29] While some studies have shown that surface topographies may promote bacterial adhesion, colonization, and biofilm formation, in addition to facilitating cell adhesion, proliferation, and new bone formation, conflicting evidence exists.[29−31] Thereby, further research is necessary to draw conclusive results. Yet, in this study, the nanostructured CoCrMo alloys maintained antibacterial properties, indicating that they could be suitable for implantation with a low risk of infection.

3.4. Cell Adhesion and Spreading. The success of an implant is largely dependent on the interactions between cells and the implanted material surfaces. Preosteoblasts and hMSCs are widely used in bone tissue engineering; therefore, we examined cell adhesion and spreading of both cell types on the CoCrMo alloys. Immunofluorescence staining showed that the MC3T3 cells on the alloys with medium and high AR nanostructures had more mature focal adhesion protein paxillin compared to the cells on the flat surface and low AR nanostructures (Figure 4A). Quantification analysis of these images confirmed that the number and size of paxillin were significantly increased on the medium and high AR nanostructures (Figure 4B,C). Furthermore, we measured the adhesive strength of MC3T3 cells on the alloy surface using a spinning disc assay, as previously reported.[26,32] The cells were sparsely seeded on the alloy surfaces to alleviate the influence of cell−cell interactions. After 1 day of culture, the spinning speed was increased stepwise, and the cells remaining on the disc were counted for a given shear stress. The number of adherent cells on the flat surface decreased significantly after the shear force was applied and continued to decrease with an increase in the shear stress. Conversely, most cells remained attached on the nanostructured alloy surfaces even when the shear stress was increased up to 63 dyn/cm^2 (Figure 4D).

The effect of the alloy nanostructures on hMSCs was similar, as shown in Figure 5. The hMSCs on the alloys with medium

https://doi.org/10.1021/acsomega.3c04305
ACS Omega 2023, 8, 47658−47666

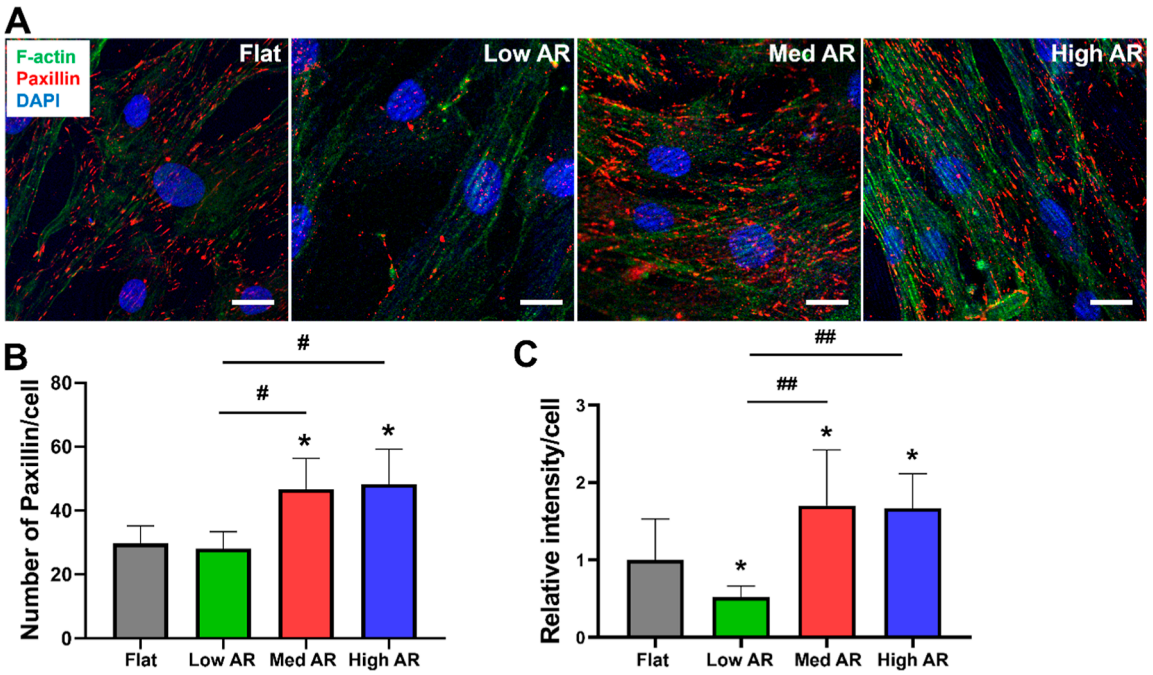

Figure 5. Adhesion and spreading of hMSCs on the samples. (A) Representative immunofluorescence images of the cells. Scale bars: 10 μm. (B) Paxillin number per cell and (C) F-actin intensity analyzed from immunofluorescence images. n = 120−300. *: $p < 0.05$ compared to the flat surface. #: $p < 0.05$, ##: $p < 0.01$ between groups.

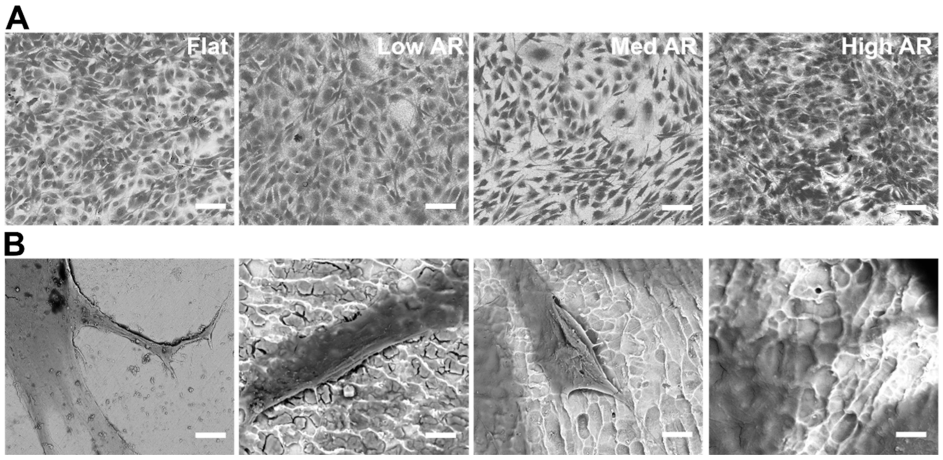

Figure 6. SEM images of hMSCs grown on the samples at (A) low and (B) high magnifications. Scale bars: 100 μm in (A) and 5 μm in (B).

and high AR nanostructures also displayed more mature paxillin and F-actin than the cells on the flat surface and low AR nanostructures. The number of paxillins and the expression of F-actin in hMSCs on the alloy surfaces with medium and high AR were significantly higher than those on the flat control surface and low AR alloy. These results indicated that the medium and high AR nanostructures promoted cell adhesion and the spreading of hMSCs. The cell morphology and interaction between hMSCs and the alloy were further inspected using SEM. The cells displayed a spreading morphology on all the surfaces (Figure 6A) and were confined onto the nanostructured surfaces (Figure 6B).

Cells can sense and respond to surface texture via focal adhesions, and nanostructures provide anchorage for cell adhesion and have a great potential to facilitate bone regeneration.[33−35] However, how cells sense underlying nanostructures is dependent on the shape and dimensions of the nanostructures.[36,37] In this study, the nanostructures were fabricated on the surface of the CoCrMo alloys via a PDP biocorrosion. Compared to the size of trough regions (several micrometers), the crests were small (~612 nm), and both MC3T3 cells and hMSCs were able to bend the cell membrane toward and confine onto the trough regions even for high AR nanostructures, as demonstrated in Figure 6. As such, the cells sensed more surface areas on the alloys with medium and high AR nanostructures than the low AR alloy and the flat surface, accompanied by increased mature focal adhesions and cell spreading. The enhanced cell-alloy surface interaction is consistent with a previous report that nanogrooves can promote cell adhesion and spreading.[38]

3.5. Osteogenic Differentiation of Preosteoblasts and hMSCs. Osteogenic differentiation is essential for the success of bone implantation as it involves the transformation of both preosteoblasts and stem cells into mature bone cells

https://doi.org/10.1021/acsomega.3c04305
ACS Omega 2023, 8, 47658−47666

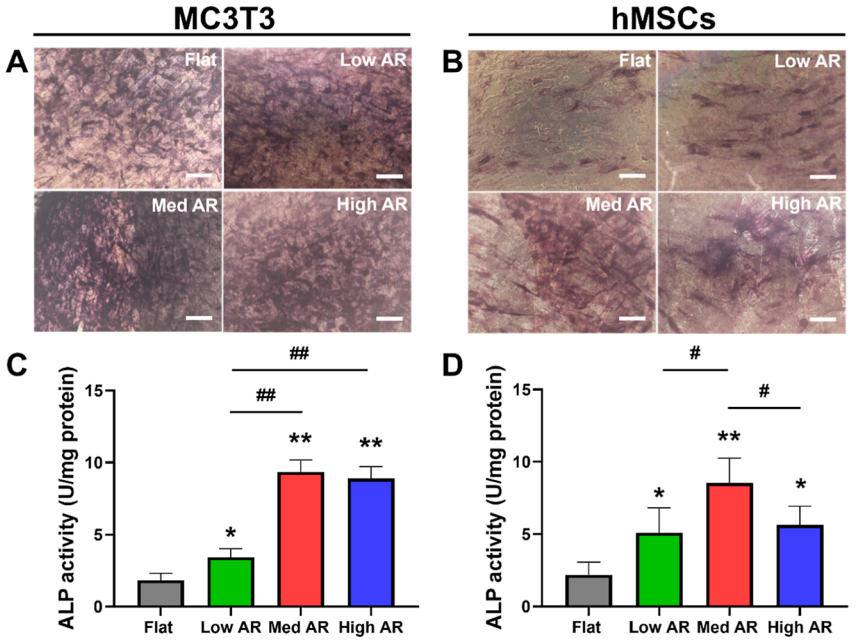

Figure 7. (A,B) ALP staining and (C,D) ALP activity of (A,C) preosteoblasts MC3T3 and (B,D) hMSCs cultured on the CoCrMo alloys. (A,B) The images are at the same scale with the scale bars of 200 μm. (C, D) $n = 3$. *: $p < 0.05$, **: $p < 0.01$ compared to the flat surface. #: $p < 0.05$, ##: $p < 0.01$ between groups.

(osteoblasts) responsible for the formation of new bone tissue.[39,40] Thus, we compared the influence of the surface nanostructures with different ARs on osteogenic differentiation of MC3T3 cells and hMSCs. The immunohistochemical staining of osteogenic differentiation marker ALP showed that medium and high AR nanostructures promoted ALP expression in both cell types (Figure 7A,B). The quantification of ALP activity further confirmed that the nanostructured surfaces, particularly the medium and high AR nanostructures, enhanced the ALP activity for both cells (Figure 7C,D). Similarly, the evaluation of cell mineralization using alizarin red S staining with MC3T3 cells also demonstrated that the medium AR nanostructure led to enhanced mineralization compared to the flat surface (Figure S2). Overall, our results showed that the nanostructures promoted osteogenic differentiation of both preosteoblasts MC3T3 cells and hMSCs, with a substantial enhancing effect for medium and high AR nanostructures.

Implant materials can serve as scaffolds to promote osteogenic differentiation by providing physical and chemical environment. Nanotopographical cues, as opposed to chemical triggers, provide a stable, precisely controlled, and safer stimuli.[41,42] Numerous studies have shown that nanostructures can affect the behavior of preosteoblasts and stem cells, including osteogenic differentiation.[16,43−45] The mechanisms underlying this effect may involve interactions of the cells with the nanotopography through focal adhesion, increase in intracellular tension, mechanotransduction pathways through cytoskeleton to nucleus, and possibly chromosome alteration.[44,46,47] Our study indicated that the medium and high AR nanostructures on the surface of CoCrMo alloys promoted osteogenic differentiation of both preosteoblasts MC3T3 cells and hMSCs. This may be attributed to the increased focal adhesion, actin fibers, and corresponding alteration of mechanotransduction.

4. CONCLUSIONS

In conclusion, this study highlights the significance of the surface nanostructures of implant materials and their impact on various biological processes. The investigation of CoCrMo alloys with surface nanostructures of various ARs has demonstrated their improved cytocompatibility, blood compatibility, and antibacterial properties. Notably, the medium and high AR nanostructures have exhibited the ability to promote both preosteoblasts and hMSCs adhesion, spreading, and osteogenic differentiation. These findings indicate the promising potential of nanostructured CoCrMo alloys as orthopedic implant materials, offering valuable insights into the development of implant materials for enhancing clinical outcomes. We acknowledged that the present study primarily focused on in vitro assessments of the nanostructured CoCr Mo alloys. To facilitate the translation of these nanostructured CoCrMo alloys into practical and reliable orthopedic implant solutions, future research efforts should encompass comprehensive in vivo investigations and long-term evaluations of their performance and potential adverse effects.

■ ASSOCIATED CONTENT

Supporting Information

The Supporting Information is available free of charge at https://pubs.acs.org/doi/10.1021/acsomega.3c04305.

Spinning disc assay setup and Alizarin red S staining of preosteoblasts MC3T3 cultured on the flat and medium AR-nanostructured CoCrMo alloys for 21 days (PDF) (PDF)

■ AUTHOR INFORMATION

Corresponding Authors

Yong Yang − *Department of Biomedical Engineering, University of North Texas, Denton, Texas 76207, United States;* orcid.org/0000-0003-4305-8029; Email: yong.yang@unt.edu

https://doi.org/10.1021/acsomega.3c04305
ACS Omega 2023, 8, 47658−47666

Narendra B. Dahotre − *Center for Agile and Adaptive Additive Manufacturing and Department of Materials Science and Engineering, University of North Texas, Denton, Texas 76207, United States*; Email: narendra.dahotre@unt.edu

Authors

Kun Man − *Department of Biomedical Engineering, University of North Texas, Denton, Texas 76207, United States; Center for Agile and Adaptive Additive Manufacturing, University of North Texas, Denton, Texas 76207, United States;* orcid.org/0000-0002-3764-3312

Sangram Mazumder − *Center for Agile and Adaptive Additive Manufacturing and Department of Materials Science and Engineering, University of North Texas, Denton, Texas 76207, United States*

Complete contact information is available at: https://pubs.acs.org/10.1021/acsomega.3c04305

Author Contributions

K.M. and S.M.: methodology, analysis, and visualization. K.M. and Y.Y.: data interpretation and writing. N.B.D. and Y.Y: conceptualization, methodology, supervision, and review.

Notes

The authors declare no competing financial interest.

■ ACKNOWLEDGMENTS

The authors acknowledge the support of the Center for Agile and Adaptive Additive Manufacturing (CAAAM) funded through State of Texas Appropriation #190405-105-805008-220 at the University of North Texas (UNT). The authors also acknowledge Nhu Nguyen for contributing to the spinning disc assay.

■ REFERENCES

(1) Kravanja, K. A.; Finšgar, M. A review of techniques for the application of bioactive coatings on metal-based implants to achieve controlled release of active ingredients. *Mater. Des.* **2022**, *217*, 110653.

(2) Amin Yavari, S.; Ahmadi, S. M.; Wauthle, R.; Pouran, B.; Schrooten, J.; Weinans, H.; Zadpoor, A. A. Relationship between unit cell type and porosity and the fatigue behavior of selective laser melted meta-biomaterials. *J. Mech. Behav. Biomed. Mater.* **2015**, *43*, 91−100.

(3) Glenske, K.; Donkiewicz, P.; Köwitsch, A.; Milosevic-Oljaca, N.; Rider, P.; Rofall, S.; Franke, J.; Jung, O.; Smeets, R.; Schnettler, R.; et al. Applications of metals for bone regeneration. *Int. J. Mol. Sci.* **2018**, *19* (3), 826.

(4) Javaid, M.; Haleem, A.; Singh, R. P.; Suman, R. Sustaining the healthcare systems through the conceptual of biomedical engineering: A study with recent and future potentials. *Biomed. Technol.* **2023**, *1*, 39−47.

(5) Chua, K.; Khan, I.; Malhotra, R.; Zhu, D. Additive manufacturing and 3D printing of metallic biomaterials. *Eng. Regen.* **2021**, *2*, 288−299.

(6) Ratner, B. D.; Hoffman, A. S.; Schoen, F. J.; Lemons, J. E. *Biomaterials Science: An Introduction to Materials in Medicine*; Academic Press: San Diego, CA, 2004; pp 162−164.

(7) Milošev, I. CoCrMo alloy for biomedical applications. *Biomedical Applications*; Springer, 2012; pp 1−72.

(8) Vidal, C. V.; Muñoz, A. I. Effect of thermal treatment and applied potential on the electrochemical behaviour of CoCrMo biomedical alloy. *Electrochim. Acta* **2009**, *54* (6), 1798−1809.

(9) Igual Muñoz, A.; Casabán Julián, L. Influence of electrochemical potential on the tribocorrosion behaviour of high carbon CoCrMo biomedical alloy in simulated body fluids by electrochemical impedance spectroscopy. *Electrochim. Acta* **2010**, *55* (19), 5428−5439.

(10) Logan, N.; Sherif, A.; Cross, A. J.; Collins, S. N.; Traynor, A.; Bozec, L.; Parkin, I. P.; Brett, P. TiO2-coated CoCrMo: Improving the osteogenic differentiation and adhesion of mesenchymal stem cells in vitro. *J. Biomed. Mater. Res., Part A* **2015**, *103* (3), 1208−1217.

(11) Batal, A.; Sammons, R.; Dimov, S. Response of Saos-2 osteoblast-like cells to laser surface texturing, sandblasting and hydroxyapatite coating on CoCrMo alloy surfaces. *Mater. Sci. Eng., C* **2019**, *98*, 1005−1013.

(12) Shen, X.; Zhang, Z.; Cheng, C.; Liu, C.; Ma, N.; Sun, D.; Li, D.; Wang, C. Bone regeneration and antibacterial properties of calcium-phosphorus coatings induced by gentamicin-loaded polydopamine on magnesium alloys. *Biomed. Technol.* **2024**, *5*, 87−101.

(13) España, F. A.; Balla, V. K.; Bose, S.; Bandyopadhyay, A. Design and fabrication of CoCrMo alloy based novel structures for load bearing implants using laser engineered net shaping. *Mater. Sci. Eng., C* **2010**, *30* (1), 50−57.

(14) Ho, Y.-H.; Man, K.; Joshi, S. S.; Pantawane, M. V.; Wu, T.-C.; Yang, Y.; Dahotre, N. B. In-vitro biomineralization and biocompatibility of friction stir additively manufactured AZ31B magnesium alloy-hydroxyapatite composites. *Bioact. Mater.* **2020**, *5* (4), 891−901.

(15) Fenoglio, I.; Fubini, B.; Ghibaudi, E. M.; Turci, F. Multiple aspects of the interaction of biomacromolecules with inorganic surfaces. *Adv. Drug Deliv. Rev.* **2011**, *63* (13), 1186−1209.

(16) Nimb, L.; Gotfredsen, K.; Steen Jensen, J. Mechanical failure of hydroxyapatite-coated titanium and cobalt-chromium-molybdenum alloy implants. An animal study. *Acta Orthop. Belg.* **1993**, *59*, 333.

(17) Dalby, M. J.; Gadegaard, N.; Tare, R.; Andar, A.; Riehle, M. O.; Herzyk, P.; Wilkinson, C. D.; Oreffo, R. O. The control of human mesenchymal cell differentiation using nanoscale symmetry and disorder. *Nat. Mater.* **2007**, *6* (12), 997−1003.

(18) Oh, S.; Daraio, C.; Chen, L. H.; Pisanic, T. R.; Finones, R. R.; Jin, S. Significantly accelerated osteoblast cell growth on aligned TiO2 nanotubes. *J. Biomed. Mater. Res., Part A* **2006**, *78* (1), 97−103.

(19) Mazumder, S.; Pantawane, M. V.; Patil, S. M.; Radhakrishnan, M.; Sharma, S.; McKinstry, M.; Dahotre, N. B. Thermokinetically Driven Microstructural Evolution in Laser-Based Directed Energy-Deposited CoCrMo Biomedical Alloy. *Adv. Eng. Mater.* **2022**, *24* (11), 2200352.

(20) Janaki Ram, G.; Esplin, C.; Stucker, B. Microstructure and wear properties of LENS deposited medical grade CoCrMo. *J. Mater. Sci.: Mater. Med.* **2008**, *19*, 2105−2111.

(21) Acharya, S.; Gopal, V.; Gupta, S. K.; Nilawar, S.; Manivasagam, G.; Suwas, S.; Chatterjee, K. Anisotropy of Additively Manufactured Co-28Cr-6Mo Influences Mechanical Properties and Biomedical Performance. *ACS Appl. Mater. Interfaces* **2022**, *14* (19), 21906−21915.

(22) Mazumder, S.; Man, K.; Radhakrishnan, M.; Pantawane, M. V.; Palaniappan, S.; Patil, S. M.; Yang, Y.; Dahotre, N. B. Microstructure enhanced biocompatibility in laser additively manufactured CoCrMo biomedical alloy. *Biomater. Adv.* **2023**, *150*, 213415.

(23) Nahian, A.; Davis, D. D. Histology, osteoprogenitor cells, *StatPearls [Internet]*; StatPearls Publishing, 2021.

(24) Marie, P. J. Osteoblasts and bone formation. *Adv. Organ Biol.* **1998**, *5*, 445.

(25) Aubin, J. E.; Triffitt, J. T. *Mesenchymal Stem Cells and Osteoblast Differentiation, Principles of Bone Biology*; Elsevier, 2002; pp 59−81.

(26) García, A. J.; Ducheyne, P.; Boettiger, D. Quantification of cell adhesion using a spinning disc device and application to surface-reactive materials. *Biomaterials* **1997**, *18* (16), 1091−1098.

(27) Rasouli, M. R.; Restrepo, C.; Maltenfort, M. G.; Purtill, J. J.; Parvizi, J. Risk factors for surgical site infection following total joint arthroplasty. *J. Bone Joint Surg.* **2014**, *96* (18), No. e158.

(28) Reichman, D. E.; Greenberg, J. A. Reducing surgical site infections: a review. *Rev. Obstet. Gynecol.* **2009**, *2* (4), 212.

(29) Teughels, W.; Van Assche, N.; Sliepen, I.; Quirynen, M. Effect of material characteristics and/or surface topography on biofilm development. *Clin. Oral Implants Res.* **2006**, *17* (S2), 68−81.

(30) Mi, G.; Shi, D.; Wang, M.; Webster, T. J. Reducing bacterial infections and biofilm formation using nanoparticles and nanostructured antibacterial surfaces. *Adv. Healthcare Mater.* **2018**, *7* (13), 1800103.
(31) Mas-Moruno, C.; Su, B.; Dalby, M. J. Multifunctional coatings and nanotopographies: toward cell instructive and antibacterial implants. *Adv. Healthcare Mater.* **2019**, *8* (1), 1801103.
(32) Gallant, N. D.; Michael, K. E.; García, A. J. Cell adhesion strengthening: contributions of adhesive area, integrin binding, and focal adhesion assembly. *Mol. Biol. Cell* **2005**, *16* (9), 4329−4340.
(33) Lavenus, S.; Ricquier, J.-C.; Louarn, G.; Layrolle, P. Cell interaction with nanopatterned surface of implants. *Nanomedicine* **2010**, *5* (6), 937−947.
(34) Goodman, S. B.; Gallo, J. Periprosthetic osteolysis: mechanisms, prevention and treatment. *J. Clin. Med.* **2019**, *8* (12), 2091.
(35) Greer, A. I. M.; Goriainov, V.; Kanczler, J.; Black, C. R. M.; Turner, L.-A.; Meek, R. M. D.; Burgess, K.; MacLaren, I.; Dalby, M. J.; Oreffo, R. O. C.; et al. Nanopatterned titanium implants accelerate bone formation in vivo. *ACS Appl. Mater. Interfaces* **2020**, *12* (30), 33541−33549.
(36) Wang, K.; Bruce, A.; Mezan, R.; Kadiyala, A.; Wang, L.; Dawson, J.; Rojanasakul, Y.; Yang, Y. Nanotopographical modulation of cell function through nuclear deformation. *ACS Appl. Mater. Interfaces* **2016**, *8* (8), 5082−5092.
(37) Shi, L.; Wang, K.; Yang, Y. Adhesion-based tumor cell capture using nanotopography. *Colloids Surf., B* **2016**, *147*, 291−299.
(38) Lu, J.; Rao, M. P.; MacDonald, N. C.; Khang, D.; Webster, T. J. Improved endothelial cell adhesion and proliferation on patterned titanium surfaces with rationally designed, micrometer to nanometer features. *Acta Biomater.* **2008**, *4* (1), 192−201.
(39) Dunlop, L. L.; Hall, B. K. Relationships between cellular condensation, preosteoblast formation and epithelial-mesenchymal interactions in initiation of osteogenesis. *Int. J. Dev. Biol.* **1995**, *39* (2), 357−371.
(40) Chen, J.; Long, F. mTORC1 signaling promotes osteoblast differentiation from preosteoblasts. *PLoS One* **2015**, *10* (6), No. e0130627.
(41) Wang, N.; Tytell, J. D.; Ingber, D. E. Mechanotransduction at a distance: mechanically coupling the extracellular matrix with the nucleus. *Nat. Rev. Mol. Cell Biol.* **2009**, *10* (1), 75−82.
(42) Widyaratih, D. S.; Hagedoorn, P.-L.; Otten, L. G.; Ganjian, M.; Tümer, N.; Apachitei, I.; Hagen, C. W.; Fratila-Apachitei, L. E.; Zadpoor, A. A. Towards osteogenic and bactericidal nanopatterns? *Nanotechnology* **2019**, *30* (20), 20LT01.
(43) Yang, Y.; Wang, K.; Gu, X.; Leong, K. W. Biophysical regulation of cell behavior—cross talk between substrate stiffness and nanotopography. *Engineering* **2017**, *3* (1), 36−54.
(44) Dobbenga, S.; Fratila-Apachitei, L. E.; Zadpoor, A. A. Nanopattern-induced osteogenic differentiation of stem cells-A systematic review. *Acta Biomater.* **2016**, *46*, 3−14.
(45) Zhang, Y.; Gong, H.; Sun, Y.; Huang, Y.; Fan, Y. Enhanced osteogenic differentiation of MC3T3-E1 cells on grid-topographic surface and evidence for involvement of YAP mediator. *J. Biomed. Mater. Res., Part A* **2016**, *104* (5), 1143−1152.
(46) Nikukar, H.; Reid, S.; Tsimbouri, P. M.; Riehle, M. O.; Curtis, A. S. G.; Dalby, M. J. Osteogenesis of mesenchymal stem cells by nanoscale mechanotransduction. *ACS Nano* **2013**, *7* (3), 2758−2767.
(47) Yang, J.; McNamara, L. E.; Gadegaard, N.; Alakpa, E. V.; Burgess, K. V.; Meek, R. M. D.; Dalby, M. J. Nanotopographical induction of osteogenesis through adhesion, bone morphogenic protein cosignaling, and regulation of microRNAs. *ACS Nano* **2014**, *8* (10), 9941−9953.

https://doi.org/10.1021/acsomega.3c04305
ACS Omega 2023, 8, 47658−47666